



Jones, T. R., Roberts, W. H. G., Steig, E. J., Cuffey, K. M., Markle, B. R., & White, J. W. C. (2018). Southern Hemisphere climate variability forced by Northern Hemisphere ice-sheet topography. *Nature*, 554(7692), 351-355. <https://doi.org/10.1038/nature24669>

Peer reviewed version

Link to published version (if available):  
[10.1038/nature24669](https://doi.org/10.1038/nature24669)

[Link to publication record in Explore Bristol Research](#)  
PDF-document

This is the author accepted manuscript (AAM). The final published version (version of record) is available online via Nature at <https://www.nature.com/articles/nature24669>. Please refer to any applicable terms of use of the publisher.

## University of Bristol - Explore Bristol Research

### General rights

This document is made available in accordance with publisher policies. Please cite only the published version using the reference above. Full terms of use are available: <http://www.bristol.ac.uk/red/research-policy/pure/user-guides/ebr-terms/>

1 **Southern Hemisphere Climate Variability Forced by Northern Hemisphere**  
2 **Ice Sheet Topography**

3

4 **T. R. Jones<sup>1\*</sup>, W. H. G. Roberts<sup>2</sup>, E. J. Steig<sup>3</sup>, K. M. Cuffey<sup>4</sup>, B. R. Markle<sup>3</sup>, J. W. C. White<sup>5</sup>**

5

6 <sup>1</sup>Institute of Arctic and Alpine Research, University of Colorado, Boulder, CO 80309-0450, USA.

7 <sup>2</sup>Bristol Research Initiative for the Dynamic Global Environment and Bristol Glaciology Centre, School of  
8 Geographical Sciences, University of Bristol, Bristol BS8 1SS, United Kingdom

9 <sup>3</sup>Department of Earth and Space Sciences, University of Washington, Seattle, WA 98195-1310, USA.

10 <sup>4</sup>Department of Geography, University of California, Berkeley, CA 94720, USA.

11 <sup>5</sup>Institute of Arctic and Alpine Research and Department of Geological Sciences, University of Colorado, Boulder,  
12 CO 80309-0450, USA.

13

14 \*corresponding author: Tyler Jones ([tyler.jones@colorado.edu](mailto:tyler.jones@colorado.edu))

15 **The presence of large Northern Hemisphere ice sheets and reduced greenhouse gas concentrations during the**  
16 **Last Glacial Maximum (LGM) fundamentally altered global ocean-atmosphere climate dynamics<sup>1</sup>. Model**  
17 **simulations and paleoclimate records suggest that glacial boundary conditions affected the El Niño-Southern**  
18 **Oscillation (ENSO)<sup>2,3</sup>, a dominant source of short-term global climate variability. Yet, little is known about**  
19 **changes in short-term climate variability at mid-to high latitudes. Here, we use an ultra-high resolution water**  
20 **isotope record from West Antarctica to demonstrate that interannual to decadal climate variability at high**  
21 **southern latitudes was almost twice as large at the LGM compared to the Holocene. Climate model**  
22 **simulations indicate that this increased variability reflects an increase in the teleconnection strength between**  
23 **the tropical Pacific and West Antarctica, owing to a shift in the mean location of tropical convection. This**  
24 **shift, in turn, can be attributed to the influence of topography and albedo of the North American ice sheets on**  
25 **atmospheric circulation. As the planet deglaciated, the largest and most abrupt decline in teleconnection**  
26 **strength occurred between ~16 and 15 ka, followed by a slower decline into the early Holocene.**

27

28 During glacial-interglacial transitions, the coupled ocean-atmosphere system shifts between stable states, driven by  
29 large climate forcings, including Milankovitch orbital cycles, greenhouse gas concentrations, and the decay of  
30 continental ice sheets<sup>1</sup>. The state changes are observed in paleoclimate proxy archives such as ice cores at high  
31 latitudes, and lake sediments and speleothems in the tropics and mid-latitudes. The state of the tropical Pacific is  
32 particularly important because this region plays a role in the generation and communication of climate anomalies  
33 between the low and high latitudes<sup>4,5</sup>.

34

35 Whether the nature of ENSO changed between the Last Glacial Maximum (LGM) and the Holocene is an important  
36 question<sup>3,6</sup>. However, proxy studies of ENSO variability during the LGM remain contradictory<sup>7,8</sup>, and the results of  
37 modeling studies are similarly ambiguous<sup>2</sup>. One obstacle to understanding past ENSO variability is disentangling  
38 changes in ENSO itself from changes in its influence on climate outside the tropics, i.e. the strength of ENSO-  
39 related teleconnections, which can vary over time<sup>9</sup>.

40

41 Tropical Pacific climate variability is an important driver of interannual to multidecadal climate variability in West  
42 Antarctica<sup>4,5</sup>. Warm sea surface temperatures (SSTs) in the tropical Pacific drive the propagation of atmospheric

43 Rossby waves towards the high latitudes, affecting weather systems that develop over the Amundsen Sea<sup>4,5</sup>.  
44 Variability in the Amundsen Sea region dominates climate variability over the adjacent West Antarctic Ice Sheet  
45 (WAIS)<sup>5,10,11</sup>. Over longer timescales, the influence of tropical climate variability on the Amundsen Sea may have  
46 implications both for the stability of the ice sheet<sup>12</sup> and for the ventilation of CO<sub>2</sub> from the Southern Ocean<sup>13</sup>.

47  
48 The influence of tropical variability on West Antarctica climate is reflected in ice core records from the WAIS. In  
49 particular, oxygen and hydrogen isotope ratios of water are sensitive to temperature and atmospheric circulation  
50 anomalies associated with large ENSO events<sup>14</sup>. Such records might therefore yield important insights about  
51 changes in tropical climate variability and tropical-to-extratropical teleconnections during glacial-interglacial  
52 transitions. In this study, we utilize a high-resolution hydrogen isotope ( $\delta D$ ) record from the WAIS Divide ice core  
53 (WDC) to investigate ~31 kyr of high-frequency climatic variability. The data were produced using laser absorption  
54 spectroscopy coupled with a continuous flow analysis system<sup>15</sup>. The record is the longest continuously-measured  
55 water isotope record ever recovered, with an effective sample resolution of 5 mm and a maximum difference in age  
56 between consecutive samples of 0.33 years.

57  
58 We use spectral techniques (see Methods) on the WDC  $\delta D$  record to analyze West Antarctic climate variability (Fig.  
59 1). Periods greater than 3 years are preserved throughout the 31 kyr record (Extended Data Fig. 1a). To account for  
60 attenuation of the  $\delta D$  signal by diffusion in the firn column and solid ice<sup>16</sup>, we apply a diffusion correction on  
61 consecutive 500-yr data windows (see Methods; Extended Data Fig. 2c). We isolate the amplitude of 3-7 and 4-15  
62 yr  $\delta D$  variations by averaging power density over these frequency ranges. The 3-7 yr range is typical of a high-  
63 frequency spectral peak seen in observations of the Southern Oscillation Index (SOI), while the 4-15 yr range is less  
64 affected by diffusion (Extended Data Fig. 1a) and captures the decadal variability observed in the SOI (Extended  
65 Data Fig. 1c), tropical Pacific coral isotope records<sup>17</sup>, and in modern observations in West Antarctica<sup>5,14</sup>.

66  
67 We find that the mean amplitudes of the diffusion-corrected variability in the 3-7 and 4-15 yr bands are elevated in  
68 the Late Glacial (16-31 ka) relative to the Holocene (0-10 ka) (Fig. 1c,d). A ~50% decrease in amplitude occurs  
69 from ~16 to 10 ka in both time series. This decline occurs in two steps: an abrupt decrease at ~16 ka followed by a  
70 second but less pronounced decline from ~13-10 ka. Neither time series reveal other significant changes in

71 variability during the Holocene or during the Late Glacial. We use an objective algorithm (see Methods) to detect  
72 initial significant decline in the diffusion-corrected 4-15 yr time series based on 500-yr data windows (Extended  
73 Data Fig. 2a,b). We find that the decline began at  $16.44 \text{ ka} \pm 0.30 \text{ kyr}$  (all ages are given relative to present = 1950  
74 C.E.). Identical results are obtained using the 3-7 yr time series. The timing of the initial decline is robust among  
75 different detection techniques. Using a sub-set of 100-yr data windows for the diffusion-corrected 4-15 yr time  
76 series (Extended Data Fig. 2c,d), the decline occurs at  $16.24 \text{ ka} \pm 0.17 \text{ kyr}$ . The timing of the decline is not an artifact  
77 of the diffusion correction. Using the raw data in the 4-15 yr band for 500-yr data windows (Fig. 1d), a  $\sim 40\%$   
78 decrease in amplitude occurs from  $\sim 16$  to  $10 \text{ ka}$ , with initial significant decline occurring at  $15.94 \text{ ka} \pm 0.30 \text{ kyr}$ .  
79 Conservatively, this places the decline in WDC variability between  $16.74$  to  $15.64 \text{ ka}$ , with a central estimate of  
80  $16.24 \text{ ka}$ .

81  
82 The climate shift at  $\sim 16 \text{ ka}$  coincides with large-scale geologic events observed in proxy records across the globe. A  
83 substantial drawdown of the Laurentide Ice Sheet (LIS) surface is estimated to have occurred at  $16 \text{ ka BP}$  (from  $^{14}\text{C}$   
84 dating)<sup>18</sup>, corresponding to the Heinrich Event 1 (H1) iceberg discharge event in the Northern Hemisphere (Fig. 2).  
85 The H1 ice rafted debris is of Laurentide origin<sup>19</sup>, indicating abrupt changes in ice mass and the topography of the  
86 LIS at this time. The Cordilleran ice sheet also declined rapidly at this time<sup>20</sup>, and the drawdown of the combined  
87 Laurentide-Cordilleran ice sheets (LCIS) has been suggested as a possible forcing mechanism for the transition from  
88 dry to wet conditions in Indonesia<sup>21</sup> (Fig. 2c). Taken together, the similarity in timing of these various records  
89 suggests a common link.

90  
91 To investigate the mechanisms responsible for changing high-frequency variability at WDC, we use the HadCM3  
92 fully-coupled ocean-atmosphere model to simulate climate in thousand-year steps from  $28$  to  $0 \text{ ka}^{22}$  (see Methods).  
93 We assess variability in both the Amundsen Sea region and the tropical Pacific. Since the isotopic composition of  
94 ice at WDC is indicative of atmospheric circulation in the Amundsen Sea region<sup>14</sup> (Fig. 3a), we examine the mid-  
95 level flow in the model, represented by the  $500 \text{ hPa}$  height field. The amplitude of the simulated variability in the  
96 mean  $500 \text{ hPa}$  geopotential height field ( $Z_{\text{ASL}}$ ) of the Amundsen Sea Low (ASL) region ( $55\text{-}70^\circ\text{S}$ ,  $195\text{-}240^\circ\text{E}$ )  
97 follows the same trend as the observations from WDC: more variability during the LGM, less variability during the  
98 Holocene, and a decline in variability at  $16 \text{ ka}$  (Fig. 4a). We examine the tropical Pacific influence ( $Z_{\text{pac}}$ ) on the

99 modeled  $Z_{ASL}$  by linearly removing the effect of the basin-wide ( $150-270^{\circ}E$ ,  $5^{\circ}N-5^{\circ}S$ ) tropical Pacific SST ( $SST_{pac}$ )  
100 from the  $Z_{ASL}$  time series (Fig. 4e,f). The amplitude of the residual ASL variability is essentially constant for the last  
101 28 kyr (Fig. 4a), demonstrating that the change in the ASL is connected to tropical variability.

102

103 The increased  $Z_{ASL}$  variability at the LGM could be the result of either increased tropical variability or a change in  
104 efficiency of the tropical-high latitude teleconnection, forced by a change in the tropical mean state. To separate  
105 these processes, we compute the strength of the teleconnection between the tropics and ASL by constructing  
106 composite maps. These composites show the average response of the 500 hPa geopotential height field to ENSO  
107 events in the tropical Pacific (see Methods). We use a composite that imposes both an upper and lower limit on the  
108 size of  $SST_{pac}$  ( $\pm 1.25$  to  $2.5$  times the pre-industrial standard deviation) to eliminate the possible influence of  
109 stronger or weaker ENSO events during the glacial period. Composites with or without this upper limit are  
110 indistinguishable. The results demonstrate that, in our HadCM3 experiments, the change in  $Z_{ASL}$  variability is the  
111 result of a more efficient teleconnection, rather than a change in ENSO variability (see Methods). A time series of  
112 the strength of the teleconnection over the last 28 ka (Fig. 2a, 4b) shows that the teleconnection is stronger through  
113 the LGM until 16 ka, at which time it rapidly decreases. This is in agreement with the modeled change in variability  
114 in  $Z_{ASL}$  and the observed timing of change in the WDC record. A change in the LGM teleconnection strength is also  
115 evident in eight out of eleven of the PMIP2/3 models (Extended Data Fig. 7). This is remarkable given the diversity  
116 of the response of these models' tropical climate to LGM forcing<sup>23</sup>.

117

118 The stronger teleconnection in the glacial period in our simulations suggests a change in the tropical Pacific mean  
119 state. Such a change could result from the lowered GHG concentrations, the altered orbital forcing, or the presence  
120 of continental ice sheets. In HadCM3, we test each of these boundary conditions individually to evaluate their  
121 impact (see Methods). The GHG concentrations and orbital forcing cause a negligible change, whereas the influence  
122 of continental ice sheets is significant. Two processes associated with continental glaciation may be important for  
123 changing the teleconnection: the lowering of sea level leading to the exposure of the shelf seas in the West  
124 Pacific<sup>23,24</sup>, and the topographic and albedo forcing of the LCIS. When considered separately, the lowered sea level  
125 causes a small change in the teleconnection that is statistically significant only to the north of the ASL region (Fig.

126 3e). Since flooding of West Pacific shelf seas is thought to have occurred at  $\sim 13 \text{ ka}^{21}$ , this may be a possible cause of  
127 the  $\sim 13\text{-}10 \text{ ka}$  decline in WDC variability, but cannot explain the larger step change at  $\sim 16 \text{ ka}$ .

128

129 The topography and albedo of the LCIS force a large change to the teleconnection strength at  $\sim 16 \text{ ka}$ , which is  
130 statistically significant across the ASL region (Fig. 3d). This timing is consistent with major deglacial changes in the  
131 LCIS, including its drawdown<sup>18</sup>. To separate the effects of topography and albedo, we perform two tests. First, using  
132 pre-industrial settings, we introduce only the LGM-LCIS into the model. In this case we find that almost the full  
133 LGM teleconnection strength change is realized (Fig. 3d). Second, we remove the LGM-LCIS topographic effect,  
134 while keeping the albedo effect. Here, the teleconnection pattern changes, but is not significant in the ASL region.  
135 Our results therefore demonstrate a link between the topography of the LCIS and multi-year to decadal climate  
136 variations in West Antarctica – a previously undocumented inter-polar teleconnection mechanism.

137

138 When the LCIS surface is high, the circulation in the North Pacific changes, with a persistent annual mean Aleutian  
139 Low that is deeper and farther south, a response that is consistent amongst climate models<sup>25</sup>. This weakens the mean  
140 winds in the West Pacific, causing the warm pool to expand eastward, as occurs during an El Niño event. The  
141 atmospheric convection moves with the warmer waters away from the Maritime Continent (Fig. 4c); hence, rainfall  
142 decreases in this region, consistent with the LGM drying inferred from lake sediments in Indonesia<sup>21</sup> (Fig. 2c) and  
143 stalagmites in Borneo<sup>26</sup> (Fig. 2d). The shifted convection then causes a change in the location of the atmospheric  
144 heating that occurs during ENSO events. Changing the location of this heating alters the structure of the extra-  
145 tropical Rossby waves that are excited during ENSO events, so that, when the LCIS is present, there are additional  
146 circulation anomalies in the Southern Hemisphere high latitudes. There are large changes in how the Rossby waves  
147 are forced from the tropics, but no change in how they propagate to the Southern Hemisphere. Since Rossby waves  
148 are the primary mechanism responsible for the tropical Pacific-West Antarctic teleconnection<sup>4,5</sup>, the LCIS can force  
149 a change in West Antarctic climate variability. Hence, when an ENSO event occurs during the LGM – even if it is  
150 no bigger than during the modern era – it has a larger impact on West Antarctic climate than it does during the  
151 Holocene.

152

153 Our results identify a novel influence of Northern Hemisphere ice sheet topography on the climate system. By  
154 altering the coupled ocean-atmospheric circulation, the decay of the LCIS affected the strength of interactions  
155 between the tropical Pacific and high southern latitudes, reducing interannual and decadal variability in West  
156 Antarctica by nearly half. While several abrupt climate events occur during the last 31 kyr, including Dansgaard-  
157 Oeschger events, the Bølling-Allerød, the Younger Dryas, and melt water pulse 1a<sup>24,27</sup> (Fig. 2e,f), the interannual  
158 and decadal climate variability in West Antarctica and the patterns of rainfall in the tropical west Pacific do not  
159 appear to be affected. Instead, the initial reduction in West Antarctic variability at ~16 ka corresponds to a  
160 maximum in North Atlantic ice rafted debris layers during H1<sup>18</sup>. It was this ice sheet purge that likely reduced LCIS  
161 topography beyond a critical threshold, altering the inter-hemispheric climate dynamics of the Pacific basin, even as  
162 separate abrupt climate events continued to occur in the Atlantic basin and further afield.



163 **References**

164

165 1. Broecker, W. S. & Denton, G. H. The role of ocean-atmosphere reorganizations in glacial cycles. *Geochimica et*  
166 *Cosmochimica Acta* **53**, 2465–2501 (1989).

167

168 2. Zheng, W., Braconnot, P., Guilyardi, E., Merkel, U. & Yu, Y. ENSO at 6ka and 21ka from ocean–atmosphere  
169 coupled model simulations. *Clim Dyn* **30**, 745–762 (2007).

170

171 3. Tudhope, A. W. *et al.* Variability in the El Niño-Southern Oscillation through a glacial-interglacial cycle. *Science*  
172 **291**, 1511–1517 (2001).

173

174 4. Lachlan-Cope, T. & Connolley, W. Teleconnections between the tropical Pacific and the Amundsen-  
175 Bellinghausens Sea: Role of the El Niño/Southern Oscillation. *Journal of Geophysical Research: Atmospheres* **111**,  
176 (2006).

177

178 5. Ding, Q., Steig, E. J., Battisti, D. S. & Küttel, M. Winter warming in West Antarctica caused by central tropical  
179 Pacific warming. *Nature Geoscience* **4**, 398–403 (2011).

180

181 6. Turney, C. S. M. *et al.* Millennial and orbital variations of El Niño/Southern Oscillation and high-latitude climate  
182 in the Last Glacial Period. *Nature* **428**, 306–310 (2004).

183

184 7. Sadekov, A. Y. *et al.* Palaeoclimate reconstructions reveal a strong link between El Niño-Southern Oscillation and  
185 tropical Pacific mean state. *Nature Communications* **4**, L11704 (2013).

186

187 8. Ford, H. L., Ravelo, A. C. & Polissar, P. J. Reduced El Nino-Southern Oscillation during the Last Glacial  
188 Maximum. *Science* **347**, 255–258 (2015).

189

190 9. Merkel, U., Prange, M. & Schulz, M. ENSO variability and teleconnections during glacial climates. *Quaternary*  
191 *Science Reviews* **29**, 86–100 (2010).  
192

193 10. Steig, E. J. *et al.* Warming of the Antarctic ice-sheet surface since the 1957 International Geophysical Year.  
194 *Nature* **457**, 459–462 (2009).  
195

196 11. Nicolas, J. P. & Bromwich, D. H. Climate of West Antarctica and influence of marine air intrusions\*. *Journal of*  
197 *Climate* **24**, 49–67 (2011).  
198

199 12. Steig, E. J., Ding, Q., Battisti, D. S. & Jenkins, A. Tropical forcing of Circumpolar Deep Water Inflow and outlet  
200 glacier thinning in the Amundsen Sea Embayment, West Antarctica. *Annals of Glaciology* **53**, 19–28 (2012).  
201

202 13. Anderson, R. F. *et al.* Wind-driven upwelling in the Southern Ocean and the deglacial rise in atmospheric CO<sub>2</sub>.  
203 *Science* **323**, 1443–1448 (2009).  
204

205 14. Steig, E. J. *et al.* Recent climate and ice-sheet changes in West Antarctica compared with the past 2,000 years.  
206 *Nature Geoscience* **6**, 372–375 (2013).  
207

208 15. Jones, T. R. *et al.* Improved methodologies for continuous-flow analysis of stable water isotopes in ice cores.  
209 *Atmospheric Measurement Techniques* **10**, 617–632 (2017a).  
210

211 16. Jones, T. R. *et al.* Water isotope diffusion in the WAIS Divide ice core during the Holocene and last glacial.  
212 *Journal of Geophysical Research: Earth Surface* **122**, 290–309 (2017b).  
213

214 17. Urban, F. E., Cole, J. E. & Overpeck, J. T. Influence of mean climate change on climate variability from a 155-  
215 year tropical Pacific coral record. *Nature* **407**, 989–993 (2000).  
216

- 217 18. Stern, J. V. & Lisiecki, L. E. North Atlantic circulation and reservoir age changes over the past 41,000 years.  
218 *Geophysical Research Letters* **40**, 3693–3697 (2013).  
219
- 220 19. Dyke, A. S. *et al.* The Laurentide and Innuitian ice sheets during the Last Glacial Maximum. *Quaternary*  
221 *Science Reviews* **21**, 9–31 (2002).  
222
- 223 20. Porter, S. C. & Swanson, T. W. Radiocarbon age constraints on rates of advance and retreat of the Puget Lobe of  
224 the Cordilleran Ice Sheet during the last glaciation. *Quaternary Research* **50**, 205–213 (1998).  
225
- 226 21. Russell, J. M. *et al.* Glacial forcing of central Indonesian hydroclimate since 60,000 y BP. *Proceedings of the*  
227 *National Academy of Sciences* **111**, 5100–5105 (2014).  
228
- 229 22. Singarayer, J. S. & Valdes, P. J. High-latitude climate sensitivity to ice-sheet forcing over the last 120kyr.  
230 *Quaternary Science Reviews* **29**, 43–55 (2010).  
231
- 232 23. DiNezio, P. N. & Tierney, J. E. The effect of sea level on glacial Indo-Pacific climate. *Nature Geoscience* **6**,  
233 485–491 (2013).  
234
- 235 24. Deschamps, P. *et al.* Ice-sheet collapse and sea-level rise at the Bølling warming 14,600 years ago. *Nature* **483**,  
236 559–564 (2012).  
237
- 238 25. Yanase, W. & Abe-Ouchi, A. A numerical study on the atmospheric circulation over the midlatitude north  
239 Pacific during the Last Glacial Maximum. *Journal of Climate* **23**, 135–151 (2010).  
240
- 241 26. Partin, J. W., Cobb, K. M., Adkins, J. F., Clark, B. & Fernandez, D. P. Millennial-scale trends in west Pacific  
242 warm pool hydrology since the Last Glacial Maximum. *Nature* **449**, 452–455 (2007).  
243

- 244 27. Johnsen, S. J. *et al.* Oxygen isotope and palaeotemperature records from six Greenland ice-core stations: Camp  
245 Century, Dye-3, GRIP, GISP2, Renland and NorthGRIP. *Journal of Quaternary Science* **16**, 299–307 (2001).  
246
- 247 28. Waelbroeck, C. *et al.* Sea-level and deep water temperature changes derived from benthic foraminifera isotopic  
248 records. *Quaternary Science Reviews* **21**, 295–305 (2002).  
249
- 250 29. Hemming, S. R. Heinrich events: massive Late Pleistocene detritus layers of the North Atlantic and their global  
251 climate imprint. *Reviews of Geophysics* **42**, 725 (2004).  
252
- 253 30. Peltier, W. R. Global glacial isostasy and the surface of the ice-age Earth: the ICE-5G (VM2) model and  
254 GRACE. *Annu. Rev. Earth Planet. Sci.* **32**, 111–149 (2004).  
255

256 **Supplementary Information** is available in the online version of the paper.

257

## 258 **Acknowledgements**

259 This work was supported by US National Science Foundation (NSF) grants 0537593, 0537661, 0537930, 0539232,  
260 1043092, 1043167, 1043518, and 1142166. Field and logistical activities were managed by the WAIS Divide  
261 Science Coordination Office at the Desert Research Institute, Reno, NE, USA and the University of New  
262 Hampshire, USA (NSF grants 0230396, 0440817, 0944266, and 0944348). The National Science Foundation  
263 Division of Polar Programs funded the Ice Drilling Program Office (IDPO), the Ice Drilling Design and Operations  
264 (IDDO) group, the National Ice Core Laboratory (NICL), the Antarctic Support Contractor, and the 109th New York  
265 Air National Guard. W.H.G.R. was funded by a Leverhulme Trust Research Project Grant. All HadCM3 model  
266 simulations were carried out using the computational facilities of the Advanced Computing Research Centre,  
267 University of Bristol (<http://www.bris.ac.uk/acrc/>). We wish to thank Paul J. Valdes and Joy S. Singarayer for  
268 providing their model simulations, as well as the groups that provided climate model data as part of the PMIP2/3.

269

## 270 **Author Contributions**

271 T.R.J., W.H.G.R., and E.J.S. designed the project and led the writing of the paper. T.R.J., J.W.C.W., E.J.S., and  
272 B.R.M. contributed water isotope measurements. W.H.G.R. conducted HadCM3 simulations and led model analysis.  
273 T.R.J., K.M.C., E.J.S., and J.W.C.W. developed the diffusion-correction calculations. B.R.M. contributed change  
274 point detection algorithms and power density ratio calculations. All authors discussed the results and contributed  
275 input to the manuscript.

276

## 277 **Author Information**

278 Reprints and permissions information is available at [www.nature.com/reprints](http://www.nature.com/reprints). The authors declare no competing  
279 financial interests. Readers are welcome to comment on the online version of the paper. Correspondence and  
280 requests for materials should be addressed to T.R.J. ([tyler.jones@colorado.edu](mailto:tyler.jones@colorado.edu)).

281 **Methods**

282

283 **1 Water isotope data**

284 The WDC water isotope record (Fig. 1a) was analyzed on a continuous flow analysis (CFA) system<sup>15</sup> using a Picarro  
285 Inc. cavity ring-down spectroscopy (CRDS) instrument, model L2130-i. The data are reported in delta notation  
286 relative to Vienna Standard Mean Ocean Water (VSMOW,  $\delta^{18}\text{O} = \delta\text{D} = 0\text{‰}$ ), normalized to Standard Light  
287 Antarctic Water (SLAP,  $\delta^{18}\text{O} = -55.5\text{‰}$ ,  $\delta\text{D} = -428.0\text{‰}$ ) scale. WDC is annually dated, with accuracy better than  
288 0.5% of the age between 0-12 ka, and better than 1% of the age between 12-31 ka<sup>31,32</sup>.

289

290 **2 Frequency domain analyses**

291 **2.1 Spectral conversion**

292 We use the MultiTaper method fast Fourier transform technique to calculate spectral power densities<sup>33,34</sup> of the  
293 measured water isotope time series. Similar to other paleoclimate studies<sup>35</sup>, we use the pmtm.m routine of P.  
294 Huybers (<http://www.people.fas.harvard.edu/~phuybers/Mfiles/>). Before spectral analysis, the isotope data are  
295 linearly interpolated at a uniform time interval of 0.05 yr.

296

297 **2.2 High-frequency signal attenuation**

298 High-frequency water isotope information in ice cores is attenuated by diffusion in the firn column and deep  
299 ice<sup>16,36,37,38,39,40</sup>. Frequency spectra reveal the amount of signal attenuation as declines in the amplitude of a given  
300 frequency through time, relative to lower frequencies (Extended Data Fig. 1a). For WDC, the annual signal (1 yr) is  
301 indiscernible at ages >14 ka. The 2 yr signal is indiscernible from 17-19 ka. Signals >3 yr are detectable throughout  
302 the last 31 kyr, while signals >4 yr are not substantially attenuated by diffusion (Extended Data Fig. 1a).

303

304 **2.3 Gaussian determination of diffusion lengths**

305 The quantitative effects of diffusion can be represented by the convolution of a Gaussian filter with the original  
306 water-isotope signal deposited at the surface and subsequently strained by ice deformation and firn compaction<sup>36,39</sup>  
307 (Extended Data Fig. 1b). The power density spectrum observed in the ice core record ( $P(f)$ ), after diffusion, is  
308  $P(f) = P_o(f) \exp[-(2\pi f \sigma_z)^2]$ , where  $P_o(f)$  represents the power spectrum of the undiffused signal,  $f$  is the

309 frequency  $\frac{1}{\lambda}$ ,  $\lambda$  the signal wavelength,  $z$  the depth, and  $\sigma_z$  the diffusion length. Fitting a Gaussian to  $P(f)$  defines a  
310 standard deviation,  $\sigma_f$ , with units of 1/meters. The conversion  $\sigma_z = \frac{1}{2\pi\sqrt{2}} \cdot \frac{1}{\sigma_f}$  then yields the diffusion length  $\sigma_z$  in  
311 units of meters<sup>16</sup>. The diffusion length expressed in units of time is  $\sigma_t = \frac{\sigma_z}{\lambda_{avg}}$ , where  $\lambda_{avg}$  is the mean annual layer  
312 thickness (m/yr) at a given depth (Extended Data Fig. 2c). The diffusion length quantifies the statistical vertical  
313 displacement of water molecules from their original position in the ice sheet. In the present study, we use our  
314 previously published WDC diffusion lengths, calculated for 500-yr data windows through the interval 0 – 29 ka<sup>16</sup>.

315

#### 316 **2.4 Natural log determination of diffusion length**

317 The  $\sigma_f$  variable can also be determined by using the slope of the linear regression of  $\ln(P(f))$  vs.  $f^2$ . This provides a  
318 means of estimating diffusion-length uncertainty<sup>16</sup>. Here,  $\sigma_f = \sqrt{\frac{1}{2 \cdot |m_{ln}|}}$ , where  $m_{ln}$  is the slope of the linear  
319 regression over the interval from 0.01 cycles<sup>2</sup>/m<sup>2</sup> to the value at which systematic noise from the ice core analysis  
320 system overwhelms the physical signal. The point where noise dominates appears as a “kink” or “bend” in the decay  
321 of  $\ln(P(f))$ . A maximum and minimum slope is fit within the standard deviation of the linear regression to determine  
322 an uncertainty range for  $\sigma_f$ .

323

#### 324 **2.5 Power density diffusion correction**

325 Diffusion of a water isotope signal in an ice sheet reduces the power of high-frequencies, so  $P(f)$  takes the form of  
326 quasi-red noise. Given that WDC Holocene spectra show constant power density in the frequencies largely  
327 unperturbed by diffusion (periods >4 yrs), we use a white-noise normalization to estimate the original, pre-diffusion  
328 power density spectrum. Specifically, we calculate  $P_o(f) = P \exp(4\pi^2 f^2 \sigma_t^2)$ , where  $P$  is the observed power  
329 density (per mil<sup>2</sup>·yr),  $f$  the frequency (1/yr), and  $\sigma_t$  the diffusion length (yr). We report the average power density for  
330 the diffusion-corrected 3-7 and 4-15 yr bands calculated as the integral of power density divided by the frequency  
331 range. The uncertainty on these power density diffusion corrections is determined using the uncertainty range for  
332 diffusion lengths discussed in section 2.4.

333

#### 334 **3 Change point detection**

335 We fit linear regressions to blocks of data centered on every possible point within the 3-7 and 4-15 yr relative  
336 amplitude time series, using block sizes of 2,500 to 10,000 yrs. We calculate the  $p$ -value for the  $F$ -test to determine  
337 whether the slope of the regression of each block is statistically different than zero (Extended Data Fig. 2b). We  
338 make no *a priori* assumptions about the timing or size of significant change and take an *a posteriori* confidence  
339 level equivalent to 95%:  $\alpha = 1 - 0.95^{1/n}$ , where  $n$  is the number of statistical test realizations<sup>31</sup>. The first  
340 significant change occurs at 16,440 ka for the 4-15 yr diffusion-corrected data (all ages are given relative to present  
341 = 1950 C.E.). The 3-7 yr diffusion-corrected data yields identical results. The first significant change in the 4-15 yr  
342 raw data (not corrected for diffusion) occurs at 15,940 yrs.

343  
344 Uncertainty in the timing of initial change includes the spectral window resolution of 500-yrs ( $\pm 250$  yrs) and the  
345 WDC14 age scale ( $\pm 1\%$  for ages  $> 12$  ka<sup>32</sup>). For initial change centered at 16.4 ka and 15.9 ka, the age scale imposes  
346 an uncertainty of  $\pm 164$  yrs and  $\pm 159$  yrs, respectively. Adding the above in quadrature yields initial timing  
347 uncertainties of just less than  $\pm 300$  yrs. We also estimate the change point visually using a sub-set of 4-15 yr  
348 diffusion-corrected data, calculated using 100-yr non-overlapping windows between  $\sim 16.64$  and 15.54 ka. The  
349 change occurs at 16.24 ka, with uncertainty on the window length of  $\pm 50$  yrs and a dating uncertainty of  $\pm 162$  yrs.  
350 Added in quadrature, this gives an uncertainty value of  $\pm 170$  yrs.

351

## 352 **4 HadCM3 model simulations**

### 353 **4.1 Model setup**

354 We use the fully coupled ocean-atmosphere model HadCM3<sup>41,42</sup>. This model has been shown to simulate the climate  
355 in the tropical Pacific very well, including in its response to glacial forcing<sup>23</sup>. We simulate the climate over the last  
356 28 ka in a series of snapshots run every 1 kyr<sup>22</sup>. For each snapshot, we prescribe the orbital forcing<sup>43</sup>, greenhouse gas  
357 (GHG) concentration<sup>44,45</sup>, and ice sheet topography and sea level<sup>30</sup>. We use a suite of simulations to test the  
358 sensitivity of the model to individual boundary conditions, including *Full 28-0 ka*, *Full 21 ka*, *21 ka orbit + GHG*,  
359 *21 ka ice sheets*, *LCIS albedo + topography* (where LCIS is the combined Laurentide-Cordilleran ice sheets), *21 ka*  
360 *West Pacific shelf exposure*, and *LCIS albedo*. Each of these simulations is defined in the Supplementary  
361 Information Data spreadsheet. All simulations are run for at least 500 years with analysis made on the final 200  
362 years of each simulation.



363

## 364 **4.2 Amundsen Sea Low variability**

### 365 **4.2.1 Long-term evolution**

366 The variability in the WDC water isotope record on interannual and longer timescales is related to changes in the  
367 large-scale atmospheric circulation, particularly in the Amundsen Sea Basin<sup>14</sup> (Fig. 3a). These changes in the  
368 circulation can be characterized by the Amundsen Sea Low (ASL)<sup>46,47</sup>. To assess the amount of variability in the  
369 ASL, we compute an *ASL index* of monthly mean 500 hPa height averaged from 55°-70°S and 195°-240°E ( $Z_{ASL}$ ).  
370 We use a 4-15 yr band-pass filter to isolate variability on the same timescale as the WDC record. Extended Data  
371 Figure 3 shows the variance of  $Z_{ASL}$  within each 1 kyr snapshot, using the *Full 28-0 ka* simulations. From 28 ka until  
372 around 15 ka, the ASL is more variable than during the Holocene (95% significant, F-test). Both the magnitude and  
373 timing of the decrease are comparable to those observed in the WDC water isotope record.

374

### 375 **4.2.2 Internal vs. forced variability**

376 To assess how much of the change in the simulated  $Z_{ASL}$  is due to the tropics, we linearly remove the average of SST  
377 across 5°N-5°S and 150-270°E ( $SST_{pac}$ ) from the  $Z_{ASL}$ . This operation is performed by regressing  $Z_{ASL}$  onto  $SST_{pac}$ ,  
378 as shown by the equation  $Z_{pac} = SST_{pac} * regress(SST_{pac}, Z_{ASL})$ . We then subtract  $Z_{pac}$  from  $Z_{ASL}$  to obtain the  
379 component of  $Z_{ASL}$  that is unrelated to the tropical Pacific:  $Z_{local} = Z_{ASL} - Z_{pac}$ . The variance of  $Z_{local}$  is plotted in  
380 Extended Data Figure 3. The results show that there is no statistically significant change in the ASL variability that  
381 is unrelated to tropical Pacific SST over the deglaciation (95% significant, F-test). We compare these results,  
382 obtained with 4-15 yr band pass filtered data of monthly mean model output, to annual mean data with no filtering  
383 (Extended Data Fig. 3a,b). We obtain very similar results for both outputs. The tests described below use the annual  
384 mean data.

385

## 386 **4.3 The tropical Pacific-to-ASL teleconnection**

387 The tropical Pacific-to-ASL teleconnection has been well documented<sup>48,49</sup>. To show this teleconnection in HadCM3,  
388 we construct composite maps of 500 hPa height for years when the annual  $SST_{pac}$  anomaly exceeds  $\pm 0.81$  °C  
389 (Extended Data Fig. 4). This threshold is chosen so that  $SST_{pac}$  anomalies exceed 1.25 standard deviations in a pre-  
390 industrial simulation. We include cold ENSO events by multiplying the 500 hPa height field by (-1). Note that

391 computing  $SST_{pac}$  over the entire tropical Pacific basin eliminates biases that may arise from changes in the pattern  
392 of SST variability, either in response to forcing or as a result of intrinsic ENSO variability.

393

394 The pre-industrial composite pattern that we obtain for the atmospheric response to tropical Pacific SST shows  
395 greatest amplitude in the Amundsen Sea region, with a positive height anomaly for warm ENSO events (Extended  
396 Data Fig. 4a). A similar pattern is obtained from reanalysis data using either regression analysis<sup>48</sup> or  
397 compositing<sup>48,50</sup>. The composite is statistically significant across the Southern Hemisphere.

398

399 Using HadCM3, we find a similar composite pattern for the pre-industrial (Extended Data Fig. 4a) and *Full 21 ka*  
400 (Extended Data Fig. 4b). The difference between the two patterns is shown in Extended Data Figure 4c; a Rossby-  
401 wave response emanating from the western tropical Pacific is evident. This response is consistent with other studies  
402 that show the tropical Pacific-to-ASL teleconnection<sup>4,5,48,51</sup>. Using each snapshot in the *Full 28-0 ka* simulations, we  
403 evaluate the amplitude of the tropical Pacific-to-ASL teleconnection as the mean of the composite averaged over 55-  
404 70°S and 195-240°E (Extended Data Fig. 5). There is a dramatic decrease in the strength of the teleconnection  
405 around 16 ka.

406

#### 407 **4.4 Teleconnection changes resulting from ENSO changes**

##### 408 **4.4.1 Results from HadCM3 experiments**

409 We find that the simulated variance of  $SST_{pac}$  anomalies at 21 ka ( $\sigma=0.78^{\circ}\text{C}$ ) is increased by 40% compared to the  
410 pre-industrial ( $\sigma=0.65^{\circ}\text{C}$ ). To determine the effect of SST variability on the teleconnection strength, we re-compute  
411 the composites using  $SST_{pac}$  anomalies in the range  $\pm 0.81^{\circ}\text{C} < SST_{pac} < \pm 1.63^{\circ}\text{C}$ , corresponding to  $SST_{pac}$  at 0 ka  
412 of  $\pm 1.25\sigma$  to  $\pm 2.5\sigma$ . By imposing both an upper and lower bound, the atmospheric response in the 500 hPa height  
413 composites is unaffected by the amplitude of simulated ENSO events. Furthermore, any change in the frequency of  
414 ENSO events is rendered unimportant by taking an average composite of events.

415

416 The composite patterns for all simulations from 28 ka to 0 ka, as well as their difference with the pre-industrial, are  
417 unchanged by imposing the upper and lower bound, while the amplitude of the composites is slightly reduced. For  
418 the *Full 21 ka simulation*, the average amplitude of the  $Z_{ASL}$  is 32 m without the upper bound, and 30 m with the

419 upper bound imposed (Extended Data Fig. 6). Therefore, even though HadCM3 simulates an increase in the strength  
420 of ENSO during the LGM, this is not the primary cause for the change in  $Z_{ASL}$  variability. Rather, the increased  $Z_{ASL}$   
421 variability occurs because the atmospheric response to  $SST_{pac}$  during the glacial period is stronger than during the  
422 pre-industrial.

423

#### 424 **4.4.2. Results from Paleoclimate Model Intercomparison Project**

425 For a subset of PMIP2/3 simulations (those for which sufficient data was available<sup>52</sup>), we follow the same procedure  
426 as outlined above to construct composites of 500 hPa height response to  $SST_{pac}$  anomalies. We include both the  
427 lower and upper  $SST_{pac}$  bounds. The composites are computed for pre-industrial and the *Full 21 ka* simulations  
428 (Extended Data Fig. 7). A change in the tropical Pacific-to-ASL teleconnection is apparent in many of the models.  
429 Since each model has a different teleconnection in the pre-industrial, the response of the models to 21 ka boundary  
430 conditions is also different.

431

432 At 21 ka, PMIP2/3 models with enhanced  $SST_{pac}$  variance do not display a consistently different teleconnection  
433 compared to models with reduced  $SST_{pac}$  variance. This confirms that changes in the tropical Pacific-to-ASL  
434 teleconnection strength are not driven by changes in the amplitude of  $SST_{pac}$  anomalies (i.e. ENSO). Indeed, in  
435 comparison to HadCM3, the most similar change in the teleconnection occurs in FGOALS-1.0g simulations.  
436 FGOALS-1.0g shows a large decrease in ENSO strength at 21 ka, compared to the HadCM3 increase. The  
437 FGOALS-1.0g positive geopotential height anomaly is shifted eastward, consistent with the location of the regional  
438 low-pressure center in the pre-industrial simulations.

439

#### 440 **4.5 Boundary condition changes responsible for the teleconnection change**

441 In *Full 21 ka* simulations, a number of the climate forcings are changed significantly compared to the pre-industrial.  
442 These include insolation, the greenhouse gas (GHG) concentrations, and the size of the ice sheets (Extended Data  
443 Fig. 8a). We investigate the impact of each of these boundary condition changes on the teleconnection. The *21 ka*  
444 *orbit + GHG* simulation does not cause a significant change (Extended Data Fig. 8b). In the *21 ka ice sheets*  
445 simulation, which includes reduced sea level, enhanced albedo in the higher latitudes, and altered topography over  
446 North America and Europe, there is a large change in the amplitude of the teleconnection (Extended Data Fig. 8c).

447 Prior modeling simulations have explored other aspects of the topographic effects of Northern Hemisphere ice  
448 sheets<sup>53</sup>, including their influence on glacial climate<sup>54</sup>, abrupt glacial climate change<sup>55</sup>, the Atlantic Meridional  
449 Overturning Circulation<sup>56</sup>, and Heinrich Events<sup>57</sup>.

450  
451 The *LCIS albedo + topography* simulation displays a significant change in the teleconnection strength, similar in  
452 magnitude to the *Full 21 ka* simulation (Extended Data Fig. 8e). The *LCIS albedo* simulation (i.e. albedo only)  
453 displays a statistically significant change in the teleconnection, but its effect is much smaller than that of topography  
454 and albedo combined (Extended Data Fig. 8f). Although we cannot isolate the effect of topography alone, our results  
455 suggest topography is the dominant mechanism acting to change the teleconnection strength. This agrees with the  
456 WDC shift in variability at ~16 ka, which is concurrent with the abrupt lowering of the LCIS<sup>18</sup>.

457  
458 It has been proposed that lowered sea level in the West Pacific at the LGM can have a large impact on tropical  
459 Pacific climate by exposing the continental shelves<sup>23,58</sup>. We test this by changing only the land-sea mask in the West  
460 Pacific in the *21 ka West Pacific shelf exposure* simulation (Extended Data Fig. 8d). This results in a change to  $Z_{ASL}$   
461 that is 3 to 4 times smaller than that seen in *LCIS albedo + topography* simulation. There is also a statistically  
462 significant change in the composite map to the north of the ASL. In the WDC diffusion-corrected variability (3-7  
463 and 4-15 yr bands), there appears to be a step-change that occurs at ~13 ka. This timing is consistent with the  
464 flooding of the continental shelves in the West Pacific<sup>24,59</sup>. Therefore, it is possible that the WDC data is detecting  
465 flooding of the continental shelves, but this effect is secondary to the abrupt change at ~16 ka.

466

#### 467 **4.6 Climatic changes associated with the teleconnection change**

468 The tropical Pacific-to-ASL teleconnection can be considered as a Rossby Wave response to diabatic heating in the  
469 western tropical Pacific<sup>60</sup>. The location of this diabatic heating will depend upon the mean state. To understand how  
470 the mean state changes, we analyze how the patterns of precipitation and SST change in the 21 ka simulations  
471 relative to the pre-industrial. Extended Data Figure 9a shows the precipitation difference between the *Full 21 ka*  
472 simulation and the pre-industrial. There is a prominent decrease in precipitation over the Maritime Continent, and an  
473 increase in precipitation over the Indian Ocean and the west and central tropical Pacific. This is consistent with  
474 proxy evidence<sup>21,23,61</sup>. In Extended Data Figure 9b, the *21 ka ice sheets* simulation accounts for the majority of the

475 precipitation changes in the *Full 21 ka* simulation. When we decompose this effect, the *LCIS albedo + topography*  
476 simulation accounts for most of the precipitation changes in the west and central tropical Pacific (Extended Data Fig.  
477 9c), while the *21 ka West Pacific shelf exposure* simulation accounts for most of the precipitation changes over the  
478 Maritime Continent and in the Indian Ocean (Extended Data Fig. 9d). We find that there is a much larger change in  
479 West Pacific diabatic heating (as shown by the precipitation field) in the *LCIS albedo + topography* simulation than  
480 in the *21 ka West Pacific shelf exposure* simulation. Since the ASL responds to diabatic heating anomalies in the  
481 West Pacific, rather than the Indian Ocean, this is consistent with our interpretation that the LCIS dominates the  
482 tropical Pacific-to-ASL teleconnection strength change. The timing of the change in the precipitation pattern is  
483 shown in Fig. 4c. At 16 ka, the location of the tropical precipitation moves westward from its glacial position to its  
484 pre-industrial position in the far west Pacific.

485

486 The location of diabatic heating is ultimately a response to the winds and SST. Extended Data Fig. 9 shows that the  
487 SST patterns for the *Full 21 ka*, *21 ka ice sheets*, and *LCIS albedo + topography* simulations are all similar.

488 Although the global mean SST is much cooler in the *Full 21 ka* simulation (Extended Data Fig. 9a), it is the spatial  
489 structure of the SST that determines the climatic response<sup>62</sup>. Thus it is not surprising that all three simulations alter  
490 the teleconnection in a similar way. Furthermore, the SST pattern is consistent across most of the 21 ka PMIP2/3  
491 simulations, indicating a robust SST response to an ice sheet. The SST pattern in the *Full 21 ka* simulation is  
492 associated with cyclonic flow in the North Pacific that is forced by the presence of the LCIS. Prior modeling has  
493 shown that this wind response to the LCIS could result from a summertime weakening of the sub-tropical high and a  
494 wintertime deepening of the Aleutian Low<sup>62</sup>.

495

## 496 **5 Data availability**

497 The WDC water isotope data that support the findings of this study are available  
498 at <http://gcmd.gsfc.nasa.gov/search/Metadata.do?entry=NSF-ANT10-43167#metadata>. Additional supporting data,  
499 including model results, are provided in the Supplementary Information Data spreadsheet and the Extended Data.

500

501

502 **Methods References**

503

504 31. WAIS Divide Project Members. Onset of deglacial warming in West Antarctica driven by local orbital forcing.  
505 Nature 500, 440–444 (2013).

506

507 32. Sigl, M. *et al.* The WAIS Divide deep ice core WD2014 chronology – Part 2: annual-layer counting (0–  
508 31 ka BP). *Climate of the Past* **12**, 769–786 (2016).

509

510 33. Thomson, D. J. Spectrum estimation and harmonic analysis. *Proceedings of the IEEE* **70**, 1055–1096 (1982).

511

512 34. Percival, D. B., & Walden, A. T. *Spectral Analysis for Physical Applications*, 583 pp., Cambridge Univ.  
513 Press, New York (1993).

514

515 35. Markle, B. R. *et al.* Global atmospheric teleconnections during Dansgaard–Oeschger events. *Nature Geoscience*  
516 **10**, 36–40 (2017).

517

518 36. Johnsen, S. J., Stable isotope homogenization of polar firn and ice, *Proceedings of Symposium on Isotopes and*  
519 *Impurities in Snow and Ice*, IAHS-AISH Publ. **118**, 210–219 (1977a).

520

521 37. Whillans, I. M. & Grootes, P. M. Isotopic diffusion in cold snow and firn. *Journal of Geophysical Research* **90**,  
522 3910–3918 (1985).

523

524 38. Cuffey, K. M. & Steig, E. J. Isotopic diffusion in polar firn: implications for interpretation of seasonal climate  
525 parameters in ice-core records, with emphasis on central Greenland. *Journal of Glaciology* **44**, 273–284 (1998).

526

527 39. Johnsen, S. J. *et al.* Diffusion of stable isotopes in polar firn and ice: the isotope effect in firn diffusion. Physics  
528 of ice core records, 121–140 (2000).

529

- 530 40. Gkinis, V., Simonsen, S. B., Buchardt, S. L., White, J. W. C. & Vinther, B. M. Water isotope diffusion rates  
531 from the NorthGRIP ice core for the last 16,000 years – glaciological and paleoclimatic implications. *Earth and*  
532 *Planetary Science Letters* **405**, 132–141 (2014).
- 533
- 534 41. Gordon, C. *et al.* The simulation of SST, sea ice extents and ocean heat transports in a version of the Hadley  
535 Centre coupled model without flux adjustments. *Clim Dyn* **16**, 147–168 (2000).
- 536
- 537 42. Valdes, P. J. *et al.* The BRIDGE HadCM3 family of climate models: HadCM3@Bristol v1.0. *Geosci. Model*  
538 *Dev.*, **10**, 3715–3743 (2017).
- 539
- 540 43. Berger, A. & Loutre, M. F. Insolation values for the climate of the last 10 million years. *Quaternary Science*  
541 *Reviews* **10**, 297–317 (1991).
- 542
- 543 44. Spahni, R. *et al.* Atmospheric methane and nitrous oxide of the Late Pleistocene from Antarctic ice cores.  
544 *Science* **310**, 1317–1321 (2005).
- 545
- 546 45. Loulergue, L. *et al.* Orbital and millennial-scale features of atmospheric CH<sub>4</sub> over the past 800,000 years. *Nature*  
547 **453**, 383–386 (2008).
- 548
- 549 46. Fogt, R. L. & Bromwich, D. H. Decadal variability of the ENSO teleconnection to the high-latitude south Pacific  
550 governed by coupling with the Southern Annular Mode\*. *Journal of Climate* **19**, 979–997 (2006).
- 551
- 552 47. Fogt, R. L., Bromwich, D. H. & Hines, K. M. Understanding the SAM influence on the south Pacific ENSO  
553 teleconnection. *Clim Dyn* **36**, 1555–1576 (2010).
- 554
- 555 48. Schneider, D. P., Okumura, Y. & Deser, C. Observed Antarctic interannual climate variability and tropical  
556 linkages. *Journal of Climate* **25**, 4048–4066 (2012).
- 557

558 49. Ding, Q. & Steig, E. J. Temperature change on the Antarctic Peninsula linked to the tropical Pacific\*. *Journal of*  
559 *Climate* **26**, 7570–7585 (2013).  
560

561 50. Welhouse, L. J., Lazzara, M. A., Keller, L. M., Tripoli, G. J. & Hitchman, M. H. Composite analysis of the  
562 effects of ENSO events on Antarctica. *Journal of Climate* **29**, 1797–1808 (2016).  
563

564 51. Ding, Q., Steig, E. J., Battisti, D. S. & Wallace, J. M. Influence of the tropics on the Southern Annular Mode.  
565 *Journal of Climate* **25**, 6330–6348 (2012).  
566

567 52. Braconnot, P. *et al.* Results of PMIP2 coupled simulations of the Mid-Holocene and Last Glacial Maximum -  
568 Part 2: feedbacks with emphasis on the location of the ITCZ and mid- and high latitudes heat budget. *Climate of the*  
569 *Past* **3**, 279–296 (2007).  
570

571 53. Abe-Ouchi, A. *et al.* Ice-sheet configuration in the CMIP5/PMIP3 Last Glacial Maximum experiments.  
572 *Geoscientific Model Development Discussions* **8**, 3621–3637 (2015).  
573

574 54. Ullman, D. J., LeGrande, A. N., Carlson, A. E., Anslow, F. S. & Licciardi, J. M. Assessing the impact of  
575 Laurentide Ice Sheet topography on glacial climate. *Climate of the Past* **10**, 487–507 (2014).  
576

577 55. Zhang, X., Lohmann, G., Knorr, G. & Purcell, C. Abrupt glacial climate shifts controlled by ice sheet changes.  
578 *Nature* **512**, 290–294 (2014).  
579

580 56. Zhu, J., Liu, Z., Zhang, X., Eisenman, I. & Liu, W. Linear weakening of the AMOC in response to receding  
581 glacial ice sheets in CCSM3. *Geophysical Research Letters* **41**, 6252–6258 (2014).  
582

583 57. Roberts, W. H. G., Valdes, P. J. & Payne, A. J. Topography's crucial role in Heinrich Events. *Proceedings of the*  
584 *National Academy of Sciences* **111**, 16688–16693 (2014).  
585



586 58. Di Nezio, P. N. *et al.* The climate response of the Indo-Pacific warm pool to glacial sea level. *Paleoceanography*  
587 **31**, 866–894 (2016).  
588

589 59. Hanebuth, T. Rapid flooding of the Sunda Shelf: A Late-Glacial sea-level record. *Science* **288**, 1033–1035  
590 (2000).  
591

592 60. Trenberth, K. E. *et al.* Progress during TOGA in understanding and modeling global teleconnections associated  
593 with tropical sea surface temperatures. *Journal of Geophysical Research: Oceans* **103**, 14291–14324 (1998).  
594

595 61. Carolin, S. A. *et al.* Varied response of western Pacific hydrology to climate forcings over the Last Glacial  
596 Period. *Science* **340**, 1564–1566 (2013).  
597

598 62. Yin, J. H. & Battisti, D. S. The importance of tropical sea surface temperature patterns in simulations of Last  
599 Glacial Maximum climate. *Journal of Climate* **14**, 565–581 (2001).  
600

601 63. Fudge, T. J. *et al.* Variable relationship between accumulation and temperature in West Antarctica for the past  
602 31,000 years. *Geophysical Research Letters* **43**, 3795–3803 (2016).  
603

604 **Figure Legends**

605

606 **Figure 1 | WDC high-frequency signal strength**

607 **a**, The raw, high-resolution WDC  $\delta D$  water isotope record (grey) and a 15-yr average (red). **b**, Power density ratio  
608 for 15 kyr before and after the primary shift in WDC variability (i.e. 16-31 ka relative to 0-15 ka); raw data in grey  
609 and diffusion-corrected data in orange. For centennial periodicities, the mean ratio is 1.3, whereas the mean ratio  
610 for raw and diffusion-corrected periods for the 4-15 yr band is 1.9 and 2.5, respectively. The blue and green  
611 intervals show 3-7 and 4-15 yr variability, respectively. The raw data ratio is lower than one at <3 years due to  
612 increased mean diffusion in the glacial period relative to the Holocene<sup>16</sup>. Periods >4 years are not substantially  
613 influenced by diffusion (Extended Data Fig. 1a). **c, d**, Plots of diffusion-corrected relative amplitudes using 500-yr  
614 data windows, normalized to the most recent value, for (c) 3-7 yr variability and (d) 4-15 yr variability. Dashed  
615 lines show  $1\sigma$  uncertainties (see Methods).

616

617 **Figure 2 | Indicators of oceanic and atmospheric variability**

618 **a**, Tropical Pacific-West Antarctic teleconnection strength from HadCM3 (see Fig. 3). The open red dots indicate  
619 where the teleconnection strength is 95% significantly different from the pre-industrial using a two-tailed Student's  
620 *t*-test. **b**, WDC diffusion-corrected 4-15 yr variability; dashed lines are  $1\sigma$  uncertainties (see Methods). **c, d**,  
621 Hydrologic variability recorded in (c) an Indonesian lake sediment core<sup>21</sup> and (d) Bornean stalagmites<sup>26</sup>. **e**, Relative  
622 sea level (solid line) and confidence interval (dashed lines)<sup>28</sup>, with the estimated duration of melt water pulse  
623 (MWP)  $1a^{24}$ . **f**, The NGRIP  $\delta^{18}O$  record<sup>27</sup> from central Greenland. The dashed black line represents the  $\sim 16$  ka  
624 maximum in North Atlantic ice rafted debris, corresponding to a massive freshwater discharge during  $H1^{18}$ . The  
625 grey block is the estimated duration of  $H1^{29}$ . The black arrow is the estimated timing of the flooding of the Sunda  
626 Shelf<sup>21,23,24</sup>.

627

628 **Figure 3 | HadCM3 teleconnection strength**

629 **a**, Map of the correlation coefficient ( $R^2$ ) for 500 hPa height and WAIS Divide  $\delta D$ , using the isotope enabled  
630 HadCM3 for the pre-industrial. Colors are shown for 95% statistical significance. **b, c, d, e** Composite maps of  
631 annual average 500 hPa height anomaly for ENSO events. Colors are plotted for 95% statistical significance using

632 a Monte Carlo test. The green box is the Amundsen Sea region over which we calculate the teleconnection strength  
633 from the mean 500 hPa height anomaly. The purple square is the WAIS Divide ice core site. The contour interval is  
634 5m in (b) and 2.5m in (c). Negative contours are dashed.

635

#### 636 **Figure 4 | HadCM3 Mechanistic Attribution**

637 **a**, The variance of the ASL Indices  $Z_{ASL}$  (solid line) and  $Z_{local}$  (dashed line), computed from monthly mean data that  
638 is filtered with a 4-15 yr band pass filter. The markers are unfilled if the variance of  $Z_{ASL}$  at each time slice is 95%  
639 significantly different (F-test) to that of 0 ka. At 21 ka, the orange triangle shows  $Z_{ASL}$  for 21 ka LCIS-only, and the  
640 green triangle shows  $Z_{ASL}$  for 21 ka Shelf Exposure (i.e. the effect of sea level change in the Maritime Continent  
641 region). **b**, The modeled teleconnection strength between the tropical Pacific and West Antarctica (solid red line;  
642 open red dots indicate statistically significant differences from pre-industrial). **c**, The difference in mean annual  
643 rainfall between the Central Pacific and the Maritime continent (average of 20°N-20°S, 145°E-190°E minus  
644 average of 20°N-20°S, 100°E-145°E), shown as an anomaly relative to the pre-industrial (light blue line). Also  
645 shown are the precipitation anomalies over the Maritime Continent only (dashed grey line). **d**, Northern Hemisphere  
646 ice area<sup>30</sup> (dashed green line) and average height of the LCIS<sup>30</sup> (blue line). In all panels, the dashed vertical line  
647 shows 16 ka, as in Figure 2. **e**, Map of the change in the 500 hPa height field variance between 21 ka and the pre-  
648 industrial. **f**, As in (e), except for the  $Z_{pac}$  variability that is linearly related to ENSO (i.e. the part removed from  
649  $Z_{ASL}$  to yield  $Z_{local}$ ). The green box is the Amundsen Sea region over which we calculate the ASL Indices in (a). The  
650 purple square is the WAIS Divide ice core site. The contour interval is 40 m<sup>2</sup>, with colors changing every 80 m<sup>2</sup>.  
651 Negative contours are dashed. Colors are plotted for 95% statistical significance using a Monte Carlo test.

652

653 **Extended Data Figure Legends**

654

655 **Extended Data Figure 1 | Signal Detection**

656 **a**, Relative amplitudes for 1-yr, 2-yr, 3-yr, and 4-yr periods calculated for 500-yr spectral data windows, normalized  
657 to the value for the annual signal in the most recent data window. Both the climate and diffusion affects the  
658 amplitude of these high-frequency signals. However, it is mainly the effects of diffusion that cause the loss of the  
659 annual signal at >14 ka. Similarly, the 2-yr period is lost between ~17-19 ka, when the rate of diffusion for WDC  
660 was highest<sup>16</sup>. Periods >3 yrs survive diffusion throughout the last 31 kyr. **b**, An example of a deconvolution  
661 calculation showing the observed  $\delta D$  water isotope record (i.e raw data; dotted red line), and the diffusion-  
662 corrected record (black line). While this calculation was not used for the data presented in this paper, it serves as a  
663 visual aide in understanding how the diffusion-corrected water isotope record would look in the time-domain. We  
664 performed all diffusion-correction calculations in the frequency domain to reduce uncertainty. **c**, The power density  
665 spectrum for the SOI Index from 1951-2017 (black; 95% confidence intervals in grey), compared with  
666 a red noise null hypothesis (red) calculated from the average of 100 power spectrums of synthetic data that have the  
667 same autocorrelation and variance as the SOI. The SOI has power greater than the red noise across a broad  
668 spectral peak between ~2-17 yrs, which can be subdivided into a ~2-7 yr high frequency peak and an ~8-17 yr peak.  
669 Due to the limited temporal span of modern observations, multi-decadal spectral estimates of the SOI cannot be  
670 adequately defined. **d**, Diffusion-corrected relative amplitudes using 500-yr windows of WDC water isotope data. **e**,  
671 The difference in age of consecutive 5 mm WDC water isotope samples ( $\Delta age_{5mm}$ ; blue) and a 500-yr sliding  
672 average (red). **f**, The WDC accumulation rate<sup>63</sup>, inverted. The accumulation, and by extension the  $\Delta age_{5mm}$  in (e),  
673 undergoes large changes during the deglaciation at ~18.5 ka, occurring 2.5 millennia before the change point in  
674 teleconnection strength at ~16 ka.

675

676 **Extended Data Figure 2 | Change Point Detection**

677 **a**, WDC 4-15 yr variability for 500-yr data windows (dashed lines are  $1\sigma$  uncertainties; see Methods). **b**, Regression  
678 test algorithm to determine the first significant change in the WDC 4-15 yr variability in (a). The first colored data  
679 point below the p-value significance threshold occurs at 16.44 ka. **c**, Example of the diffusion-correction calculation  
680 for a 100-yr data window centered on 15.54 ka bp; raw data (black), diffusion corrected data (blue), Gaussian fit

681 (red) with dashed  $1\sigma$  uncertainty bounds (see Methods). The same calculation is made for 500-yr data windows. **d**,  
682 The sub-set of diffusion-corrected 4-15 yr amplitudes (green) calculated at 100-yr resolution. The values are  
683 normalized to the amplitude value at 16.24 ka, which represents the change point towards smaller amplitudes.

684

### 685 **Extended Data Figure 3 | ASL variability**

686 Panels (a) and (b) show the variance of the ASL Indices  $Z_{ASL}$  (black) and  $Z_{local}$  (blue). **a**, The ASL Indices are  
687 computed from monthly mean data then filtered with a 4-15 yr band pass filter. **b**, The ASL Indices are computed  
688 from annual mean output. We compute  $Z_{ASL}$  as the mean 500 hPa height in the region  $55^{\circ}$ - $70^{\circ}$ S and  $195^{\circ}$ - $240^{\circ}$ E.  
689 The blue lines show  $Z_{ASL}$  after linearly removing the  $SST_{pac}$  time series from the 500 hPa height field; this is the ASL  
690 variability unrelated to the tropical Pacific ( $Z_{local}$ ; see Methods). The markers are unfilled if the variance of  $Z_{ASL}$  at  
691 each time slice is 95% significantly different (F-test) to that of the pre-industrial. **c**, Map of the change in the  
692 variance of the 500 hPa height field between 21 ka and the pre-industrial. **d**, The variability that is linearly related  
693 to ENSO,  $Z_{pac}$  (this is the part removed from  $Z_{ASL}$  to yield  $Z_{local}$ ). **e**, The variability with the effect of ENSO linearly  
694 removed (see Methods; this the equivalent of  $Z_{local}$ ). Changes not attributable to ENSO occur to the north of the  
695 Amundsen Sea, while changes over the Amundsen Sea are related to ENSO. In (c), (d), and (e) the contour intervals  
696 are  $40\text{ m}^2$ , with colors changing every  $80\text{ m}^2$ . Negative contours are dashed.

697

### 698 **Extended Data Figure 4 | Composites of the 500 mb height field for ENSO events**

699 Composites for **a**, the pre-industrial, **b**, Full 21ka, and **c**, the difference between Full 21ka and pre-industrial.  
700 Colors are plotted for 95% statistical significance using a Monte Carlo test. Negative contours are dashed. In (a)  
701 and (b) the contours are plotted every 5 m and colors saturate at  $\pm 25\text{ m}$ . The thin blue box shows where the ASL  
702 index is computed. In (c) contours are plotted every 2.5 m and colors saturate at  $\pm 12.5\text{ m}$ .

703

### 704 **Extended Data Figure 5 | Tropical Pacific-to-ASL teleconnection strength**

705 Computed using the Full 28-0 ka simulations. **a**, Average 500 hPa geopotential height anomaly in the Amundsen Sea  
706 region, computed within the blue box shown in Extended Data Figure 4. These values are derived from composites  
707 constructed using only the lower limits on the size of ENSO events (see Main Text and Methods). **b**, The t-score is  
708 shown by the red line. Values outside the shaded red region are 95% statistically different from the pre-industrial.

709

710 **Extended Data Figure 6 | Composites of the 500mb height field for ENSO events with and without upper bound**

711 **a**, The teleconnection without upper limit using the Full 21 ka simulation. **b**, The teleconnection with upper limit  
712 using the Full 21 ka simulation. **c**, The difference in teleconnection between the Full 21ka simulation and the pre-  
713 industrial without upper limit. **d**, The same difference as (c) with upper limit. In all panels, negative contours are  
714 dashed, and colors are plotted for 95% statistical significance using a Monte Carlo test. In (a) and (b), the contours  
715 are plotted every 5 m and colors saturate at  $\pm 25$  m. In (c) and (d), contours are plotted every 2.5 m and colors  
716 saturate at  $\pm 12.5$  m.

717

718 **Extended Data Figure 7 | Composite maps of annual average 500mb height in PMIP2/3 models**

719 For each model the top panel shows the 0 ka composite and the bottom panel the difference between the Full 21 ka  
720 and 0 ka simulation. Colors are plotted for 95% statistical significance using a Monte Carlo test. In the upper  
721 panels, contours are plotted at 5m intervals, with colors saturating at 25m. In the lower panels contours are plotted  
722 at 2.5m intervals, with colors saturating at  $\pm 12.5$  m. Negative contours are dashed. The reduced statistical  
723 significance in these panels compared to those shown in Extended Data Figures 4, 6, 8, 9, and 10 is due to the  
724 shorter data series available in the PMIP2/3 archives.

725

726 **Extended Data Figure 8 | Sensitivity of composite maps to different sets of 21ka boundary conditions**

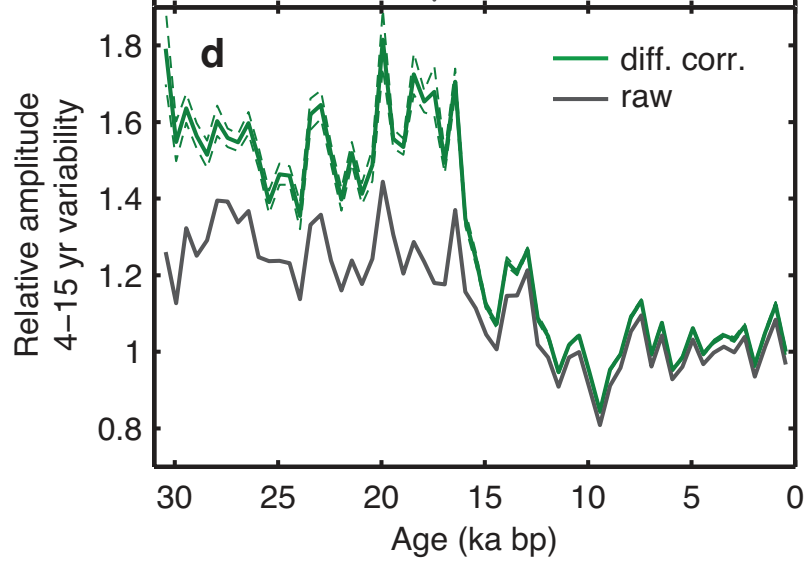
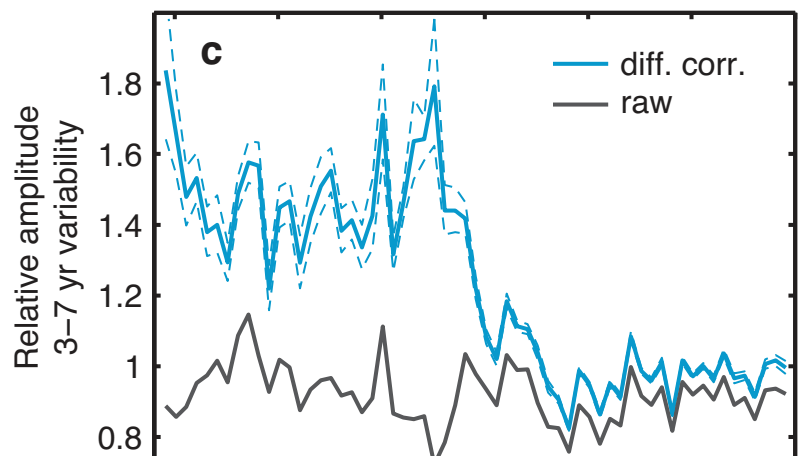
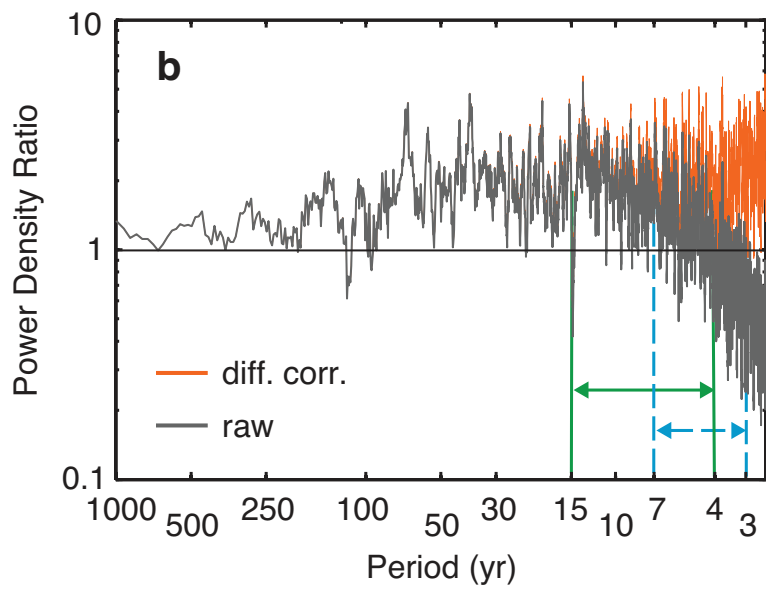
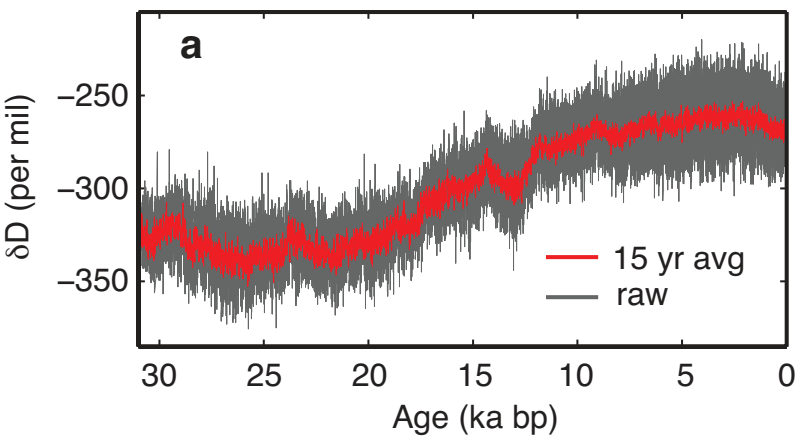
727 All plots show the difference between 21ka and 0ka composites. The composites are constructed using both upper  
728 and lower limits on the size of ENSO events. Contours are plotted every 2.5 m (negative contours are dashed) and  
729 colors saturate at  $\pm 12.5$  m. Colors are plotted for 95% statistical significance using a Monte Carlo test. **a**, Full 21  
730 ka simulation. **b**, 21 ka orbit + GHG. **c**, 21 ka ice sheets. **d**, 21 ka West Pacific shelf exposure. **e**, 21 ka LCIS albedo  
731 + topography, (where LCIS is the combined Laurentide-Cordilleran ice sheets). **f**, 21 ka LCIS albedo. Each of these  
732 simulations is fully defined in the Supplementary Information Data spreadsheet.

733

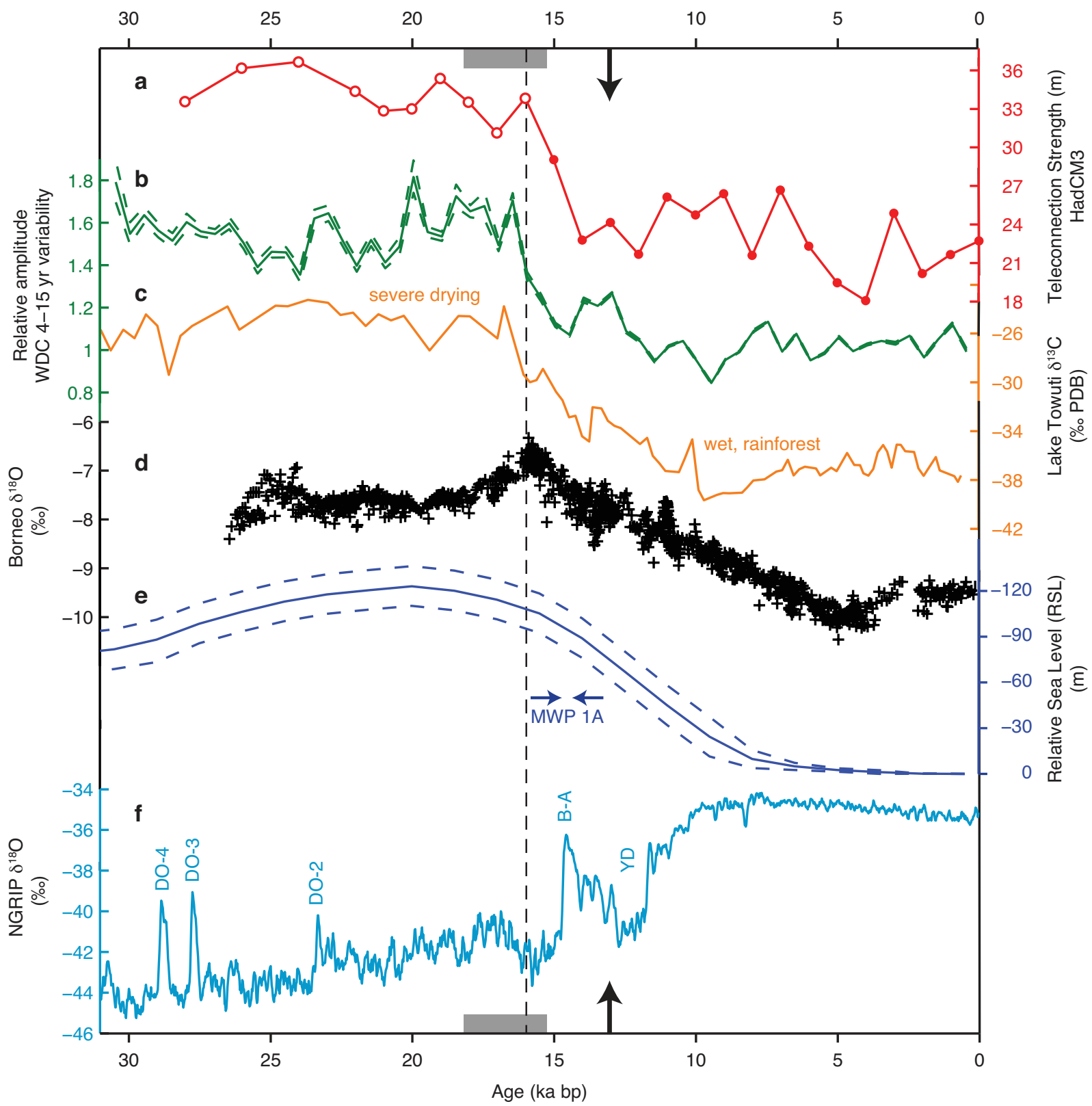
734 **Extended Data Figure 9 | Annual mean anomalies of precipitation and sea surface temperature**

735 Maps of 21 ka anomalies relative to the pre-industrial. **a**, Full 21 ka simulation. **b**, 21 ka ice sheets. **c**, 21 ka LCIS  
736 albedo + topography. **d**, 21 ka West Pacific shelf exposure. Annual means are calculated from 100 years of output.

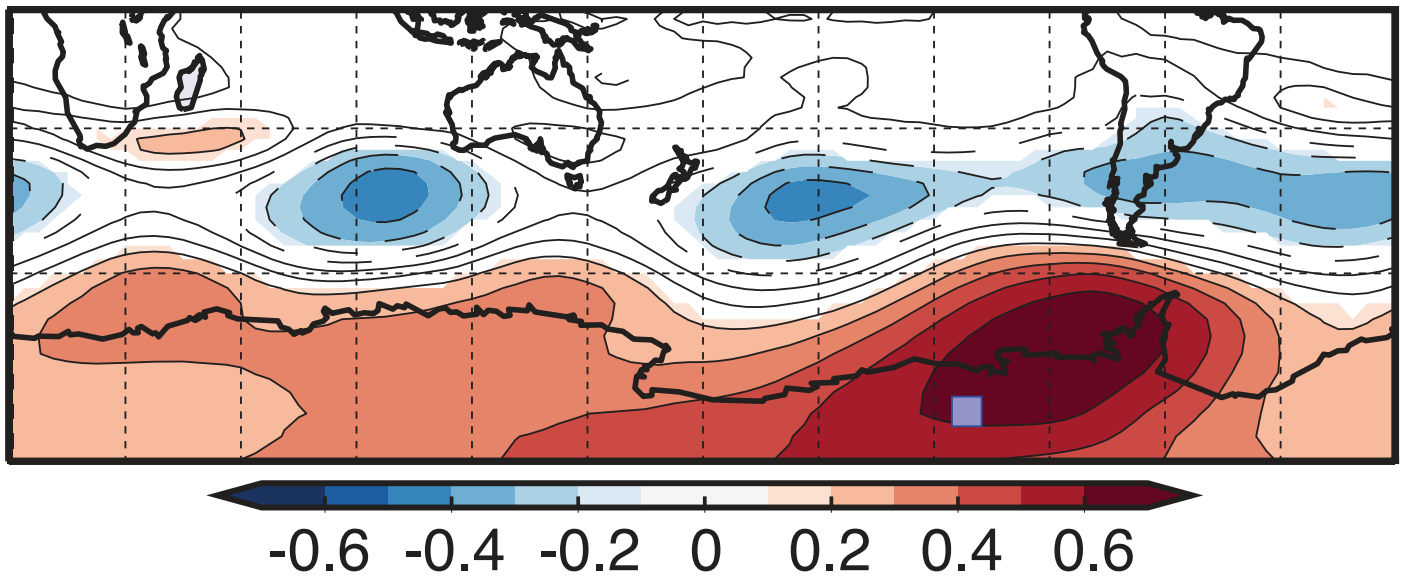
737 *Contour intervals for precipitation are 1 mm day<sup>-1</sup>, and for sea surface temperature are 0.5°C. Land areas are*  
738 *shown in in grey. Note that the temperature color scale in (a) ranges from -4 to 0 °C. This accounts for the mean*  
739 *GHG cooling that is seen in the Full 21 ka simulation.*  
740



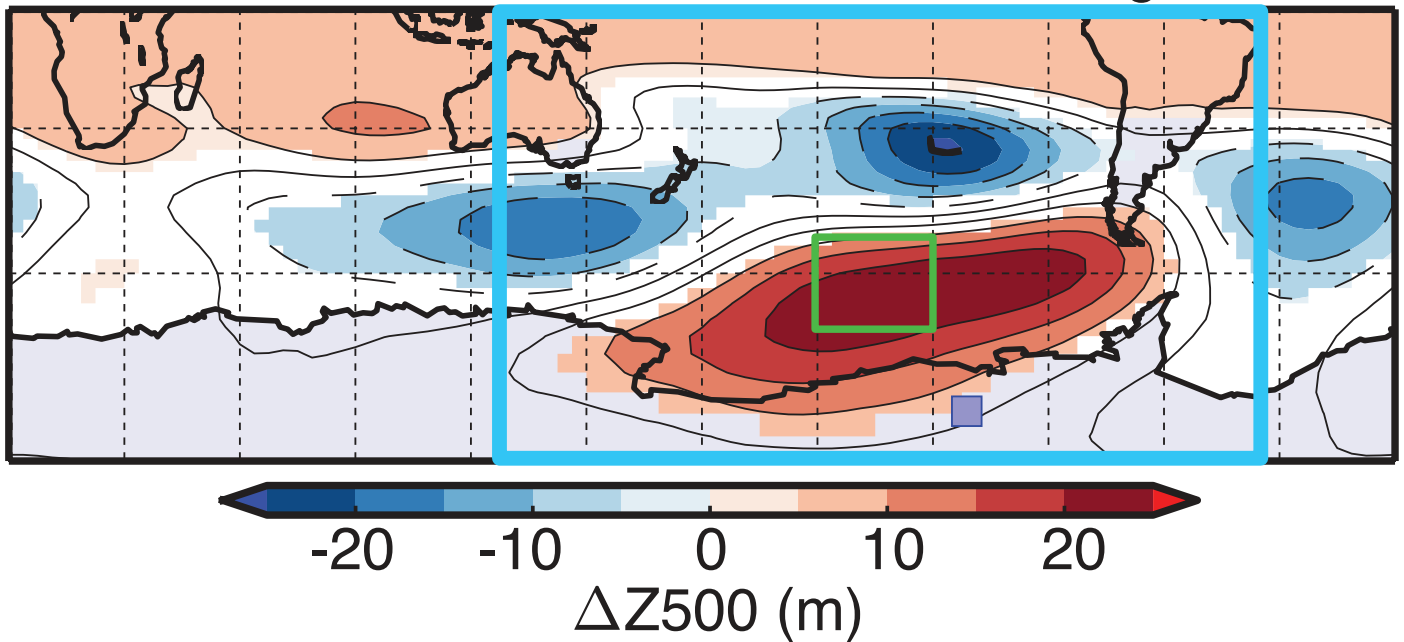




**a** Correlation ( $R^2$ ) of Z500 and WDC  $\delta D$

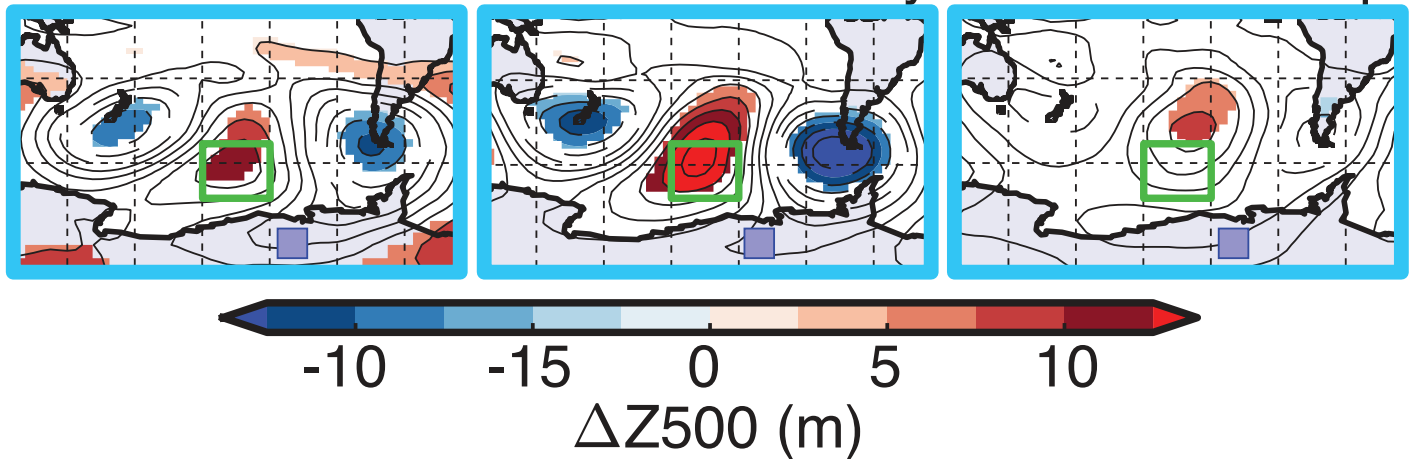


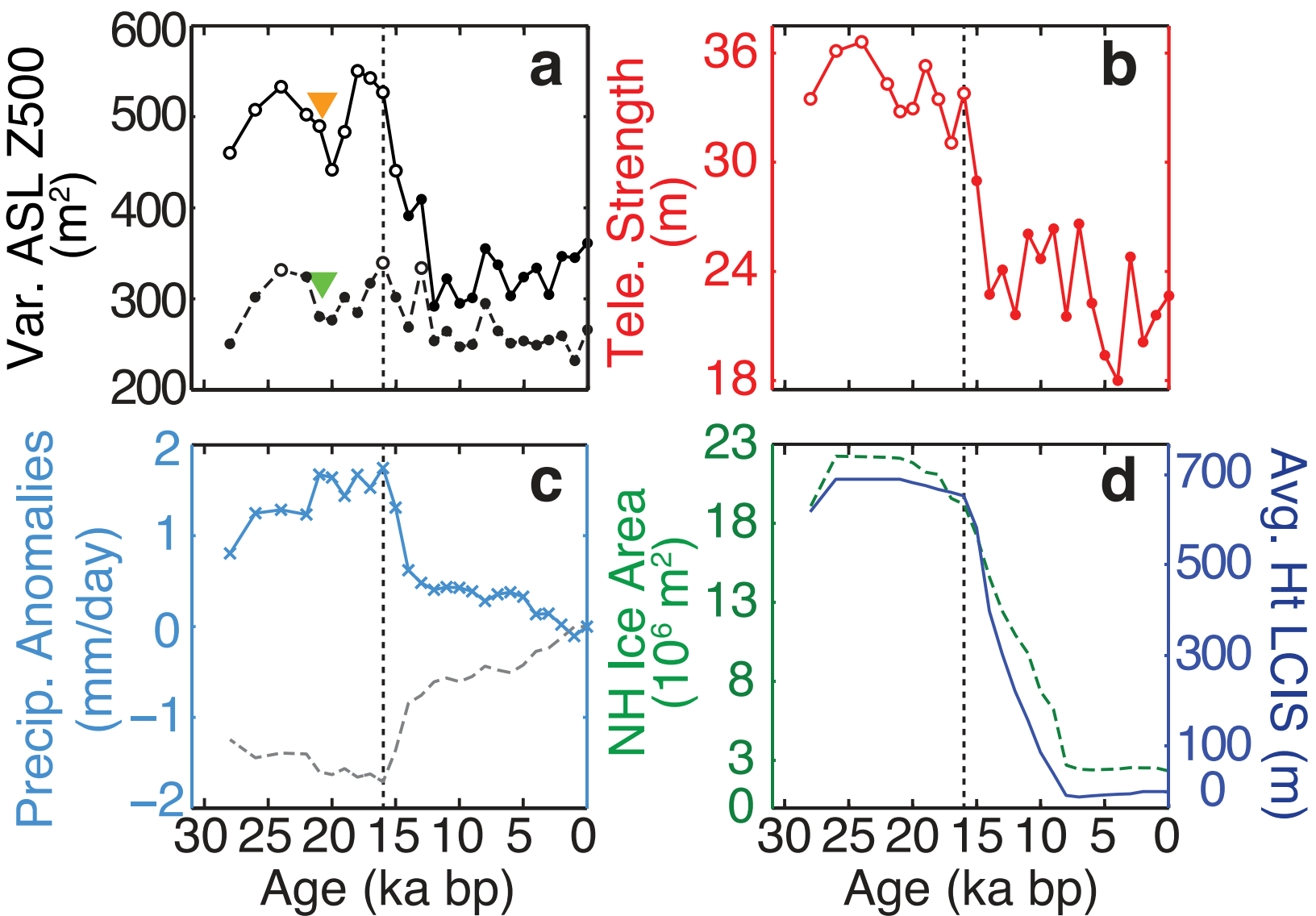
**b** Pre-Industrial Teleconnection Strength



Difference from Pre-Industrial

**c** 21ka Full **d** 21ka LCIS-only **e** 21ka Shelf Exp.





Difference from 21ka to Pre-Industrial

